Chapter 17

Ab Initio Determination of Peptide Structures by MicroED

Chih-Te Zee, Ambarneil Saha, Michael R. Sawaya, and Jose A. Rodriguez

Abstract

Structural elucidation of small macromolecules such as peptides has recently been facilitated by a growing number of technological advances to existing crystallographic methods. The emergence of electron micro-diffraction (MicroED) of protein nanocrystals under cryogenic conditions has enabled the interrogation of crystalline peptide assemblies only hundreds of nanometers thick. Collection of atomic or near-atomic resolution data by these methods has permitted the ab initio determination of structures of various amyloid-forming peptides, including segments derived from prions and ice-nucleating proteins. This chapter focuses on the process of ab initio structural determination from nano-scale peptide assemblies and other similar molecules.

Key words Peptide, Nanocrystal, Amyloid, Ab initio, Direct methods

1 Introduction

Electron micro-diffraction (MicroED) is a cryoEM technique well-suited to the determination of peptide and small macromolecule structures [1–4]. The first novel macromolecular structure solved by MicroED [5], a peptide segment of the Parkinson's-associated protein alpha synuclein, established the method's utility as a means of rapid structural analysis of crystals as small as a hundred nanometers thick. The subsequent determination of four ab initio structures of prion peptides demonstrated the approach's expediency in obtaining atomic-resolution structures of peptides [6].

Since these initial breakthroughs, the investigation of peptides by MicroED has grown and now includes over 20 structures; 14 structures at better than 1.2 Å resolution [3, 7–11]. Because of the success of ab initio methods for structural determination of peptide assemblies by MicroED [3, 6], we focus this chapter on procedures for the collection of high-resolution MicroED data from peptide nanocrystals and atomic-resolution determination of ab initio structures from said crystals. This approach hinges on the availability of well-ordered crystals hundreds of nanometers thick as

well as the concurrent use of cryogenic techniques to minimize radiation damage [1]. We demonstrate the implementation of this technique on GSNQNNF, a routinely studied heptapeptide segment of the prion protein [12], which forms needle-like crystals several microns in length but no more than a few hundred nanometers thick and wide.

As with the interrogation of larger macromolecular structures by MicroED, data collection from frozen hydrated crystals proceeds by measuring diffraction from a selected area of an illuminated crystal while that crystal is rotated unidirectionally in the electron beam [1, 13]. Diffraction movies recorded during this process are then converted into formats accessible to conventional crystallographic processing programs, which reduce MicroED data to intensities [13] used for ab initio phasing by direct methods. Solutions obtained by this approach contain collections of atoms which display correlations with the measured data. These in turn can generate electrostatic potential maps that inform the placement of residues along a polypeptide chain. Fourier difference density in these structures may reveal the positions of riding hydrogens, a feat difficult to accomplish via conventional X-ray crystallographic methods [5, 6, 14].

The procedures outlined in this chapter assume a certain degree of practical and theoretical knowledge related to operation of transmission electron microscopes, cryoEM, crystallography, and diffraction theory. For a primer on these subjects the reader is encouraged to read additional chapters in this book, or one of several recent reviews or books [1, 15–18].

2   Materials

2.1   Sample-Preparation Tools and Consumables

1. 200–400 mesh grids, covered with continuous or perforated carbon.

2. Ultra-fine grade reverse self-closing tweezers.

3. Vitrobot fine-tip tweezers.

4. Whatman No. 1 filter paper for specimen blotting and standard Vitrobot filter paper.

5. Glass petri dish with lid for grid storage and transport.

6. 2, 10, 20 μL micropipettors for sample manipulation and application.

7. Crystal slurries prepared in batch, or in hanging or sitting drops via vapor diffusion or other crystal growth and storage system.

8. Cryogen-resistant grid storage boxes with screw-top tool.

9. Personal protective equipment: several procedures require use of safety goggles, gloves, and cryogen protection including cryogen gloves and face shields.

2.2 Grid Surface Treatment

1. Several surface treatment systems are adequate [19]. We describe use of a PELCO easiGlow, glow discharge, and plasma generation system capable of 30 mA plasma currents, with vacuum control and containing a platform with a recess suited for 25 × 75 mm slide. This equipment also requires a rotary vacuum pump and gas and vent inlets.

2. Clean a standard glass micro-slide, 75 × 25 mm, 1 mm thick onto which grids can be placed for glow discharging. Other grid holders can be used instead.

2.3 Cryo Storage and Cryo-Transfer Systems

1. Several sample vitrification tools are available to perform rapid sample cooling following the Dubochet method [20, 21]. Here, we describe use of a Vitrobot Mark IV cryo-sample plunger capable of automated sample vitrification into liquid ethane.

2. While a number of sample transfer holders are available, we describe use of the Gatan 626 cryo-transfer holder with a high tilt range and low sample drift.

3. The Gatan cryo-transfer holder pairs with Gatan dry pumping station model 655 and Gatan cryo-transfer station.

2.4 Microscope Components

1. Microscope types include Tecnai series FEI microscopes such as the F20 TEM (200 keV) [13], F30 TEM (300 keV) [22], FEI Talos Arctica S/TEM (200 keV) [4] or Titan (300 keV), or JEOL JEM-3200, JEM-2200/2100 or cryo ARM series [23]. Here, we describe use of a Tecnai F30 TEM (300 keV) in microprobe mode.

2. Electron source: Field-emission gun operating with accelerating voltages in the 100–300 keV range (*see* **Note 1**).

3. Selected area aperture: Aperture diameters in the 50–150 μm range are recommended. Depending on lens system, aperture sizes can correspond to ~0.5–4.0 μm in diameter at the image plane.

4. Sample stage: Stage accuracy tilt range and tilt speed should be carefully calibrated to maintain eucentricity at the sample. Typical stage parameters include a tilt range of ±70° and tilt speed of 0.1–10°/s.

2.5 Cameras and Computing

1. Several detectors are suitable for data collection including some that have been developed specifically for MicroED. We focus on use of the TVIPS TemCam-XF416: a 16-megapixel CMOS sensor with integrated electronics delivering 16-Bit images at up to 48 frames/s with correlated double sampling [22] (*see* **Note 2**).

2. The camera is controlled by EMMenu4 with two pre-set camera recording settings. One may be a full-chip readout with subsampling by 2, the second a full-chip readout with subsampling by 4; both in rolling shutter mode.

3. Computing infrastructure is essential for both data collection and processing. Here, we describe software operating in a Linux environment on a server system powered by 40 processing threads (Intel® Xeon ® CPU E5-2680 v2 @ 2.80 GHz) with 256 GB of RAM, connected to a storage server with 400 TB of redundant (RAID6) NFS storage.

2.6 Data Reduction and Structure Determination Software

1. Data parsing and visualization software: Software for conversion of diffraction movies to crystallographic format diffraction images is limited. We describe conversion of Tietz Video Image Processing Systems (TVIPS) files to SMV format using a custom program: tvips2smv (https://cryoem.ucla.edu/pages/MicroED) [13]. Diffraction image visualization can be achieved using the Adxv program (www.scripps.edu/tainer/arvai/adxv.html) [24].

2. Data processing programs (see **Note 3**): Indexing, integration, merging, and scaling can be achieved through a variety of software programs. We describe use of the XDS package (http://xds.mpimf-heidelberg.mpg.de/) [25].

3. Ab initio structure determination is achieved using various direct methods programs. We describe use of the SHELX-97 suite, programs SHELXD and SHELXT (http://shelx.uni-ac.gwdg.de/) [26].

4. X-ray crystallographic refinement programs suitable for processing electron diffraction data must have the capacity to use electron scattering factors. Among those described here are the SHELX-97 suite [26]; Phenix suite (https://www.phenix-online.org/) [27]; CCP4 suite: REFMAC (http://www.ccp4.ac.uk/) [28].

5. Programs for dataset visualization, model building, and structural analysis include the ViewHKL program in the CCP4 suite for dataset visualization [29], the Coot model building program (https://www2.mrc-lmb.cam.ac.uk/personal/pemsley/coot/) [30] and PyMOL (https://pymol.org/2/) for model building and structure analysis [31].

3 Methods

This section provides guidance on the experimental workflow of electron diffraction of peptide nano- and microcrystals, from sample preparation to structure determination (Figs. 1 and 2).
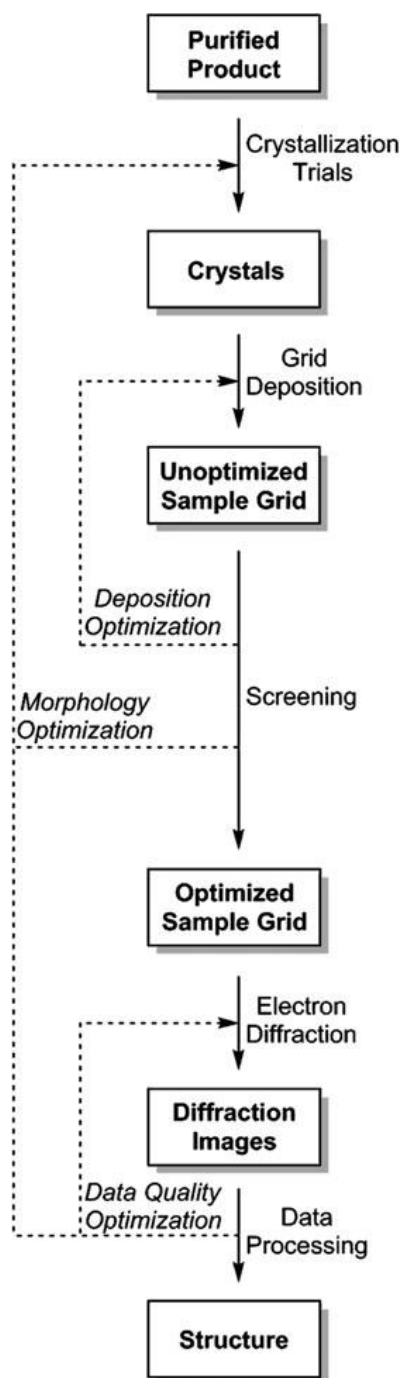
Fig. 1 General workflow of experiments to prepare samples, collect diffraction patterns, and process data for structure determination

3.1 Grid Preparation and Freezing (See Note 4)

1. Transfer EM grid from box to a clean glass slide using ultra-fine self-closing tweezers.

2. Glow discharge grid for 20–60 s per side at ~30 mA, following manufacturer's instructions.
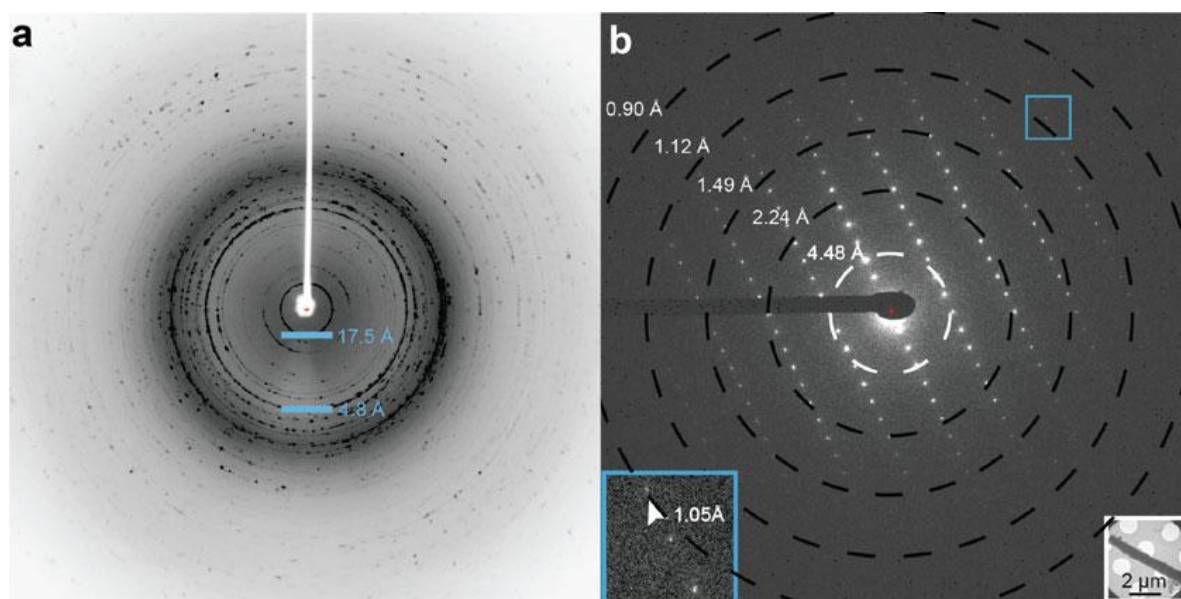
Fig. 2 X-ray powder diffraction (**a**) and single crystal MicroED pattern (**b**) of L-GSNQNNF (unit cell dimensions: $a = 4.86$ Å, $b = 14.12$ Å, $c = 17.71$ Å). The powder diffraction in **a** integrates a 5° scan of a loop filled with small crystals. Powder diffraction patterns which show gradual radial decay of signal in high-resolution regions suggest the presence of crystalline material, even if certain unit cell vectors lack an intense, corroborating ring. The pattern in **b** samples a 0.6° wedge of reciprocal space. Blue squares correspond to magnified regions of the pattern showing diffraction between 1.0 and 1.2 Å. White inset shows the over-focused image of the crystal irradiated to produce the diffraction pattern

3. Prepare Vitrobot for freezing following manufacturer's instructions, filling the sample storage reservoir with liquid nitrogen, placing a grid storage box in the liquid nitrogen reservoir, placing the copper ethane cup at its center, and linking them via a heat transfer apparatus. Condense ethane into cup following safety protocols (*see* **Note 5**).

4. Secure grid using Vitrobot tweezers and place into Vitrobot assembly following manufacturer's instructions, as per the Dubochet method [21].

5. Collect 5 μL or more of a slurry of crystal fragments of sub-micron thickness suspended in mother liquor.

6. Place 1–3 μL of crystal slurry per side, on either one or both sides of the grid (*see* **Note 6**).

7. Immediately follow Vitrobot procedures for blotting and plunge freezing of grid into liquid ethane [32] (*see* **Note 7**), then transfer the grid to a liquid nitrogen storage box.

8. Transfer grid boxes to permanent storage or to cryo holder transfer station for immediate use.

**3.2 Cryo-Transfer
(See Note 4)**

1. Cool cryo-transfer station with liquid nitrogen and transfer sample grid box containing sample grids into the transfer station sample platform.

2. Having followed procedures for preparation of the 626 cryo-transfer holder—in particular regeneration of the zeolite in the holder dewar—remove the holder from the 655 pumping station following manufacturer's instructions and place into the cryo-transfer station.

3. Fill sample holder dewar with liquid nitrogen and refill transfer holder station with liquid nitrogen to a level above the holder rod. Pull back protective copper blades to allow sample placement onto holder.

4. Remove grid from sample box and place onto sample holder with pre-cooled fine tip tweezers.

5. Place copper clip ring on top of grid and secure onto sample holder. Cover sample with protective blades.

6. Remove transfer holder from station and place into microscope CompuStage at the correct orientation, making sure to minimize the amount of time the holder spends in air.

**3.3 Grid Screening
and Preliminary
Diffraction**

1. Assuming operation of a fully calibrated instrument in microprobe mode, perform eucentric height alignment by wobbling the sample and adjusting the z-height.

2. Focus the system on the back focal plane of the objective lens by adjusting the focus knob at a magnification greater than 25,000 × while viewing the edge of a hole or a distinctive feature on the carbon support.

3. Expand the beam using the intensity knob to a near parallel state, and set spot size to 11 (*see* **Note 8**).

4. Press diffraction button on console to operate the microscope in diffraction mode. Ensure the beam is free of astigmatism (*see* **Note 9**).

5. Position the beam at the center of the detector and calibrate the location of the selected area aperture (SAA) as needed.

6. For sample detection, expand the beam by adjusting the power to the condenser lens used to focus the beam. This can be achieved, for example, by turning the intensity knob to enter overfocused diffraction mode. One could pre-set this configuration using low-dose settings. Scan the grid for crystals by moving the stage x, y location using the trackball or joystick. If available, low-dose mode can automate the focus adjustments to minimize electron exposure on samples while the grid is examined. Where low dose is available, visual inspection of the grid can be performed in overfocused diffraction under

the "focus" or "search" mode, while diffraction patterns can be recorded with the beam at crossover in "exposure" mode on an FEI microscope.

7. Find an appropriate object on the grid to use as a reference and fine-tune the specimen's eucentric height by adjusting the z-height while wobbling.

8. Diffract from a target crystal by (a) inserting the SAA; (b) inserting and adjusting the beamstop; (c) returning the beam to crossover; (d) capturing an initial diffraction pattern with an exposure ranging from 0.1 to 10 s (*see* **Note 10**); (e) repeating **steps a** to **d** as necessary to (1) assess the resolution to which the sample appears to diffract and (2) diagnose whether or not this particular crystal diffracts well enough to warrant collection of a full dataset.

9. Verify if the detector distance is appropriate for sample and adjust if necessary, using the magnification knob (*see* **Note 11**).

10. Fine-tune the z-axis height in overfocused diffraction mode while tilting the sample between the upper and lower limits planned for data collection. The crystal should always remain within the SAA throughout the desired tilt range (*see* **Note 12**).

11. To collect diffraction movies as the stage rotates from one high angle tilt to the other, initiate data recording on the camera while independently setting a stage trajectory at a desired rotation rate (*see* **Note 13**).

12. Repeat **step 11** for subsequent data collection from different samples (*see* **Note 14**).

Subheadings 3.4–3.6 provide detailed instructions to execute data processing with select software programs (Fig. 3).

3.4 Data Conversion and Processing

1. Use a script such as tvips2smv to convert raw movie files from native ".tvips" format (Tietz Video and Image Processing Systems, generic output from TemCam detectors) or other proprietary format into a series of images in standard crystallographic format (e.g., SMV, with a ".img" suffix) readable by XDS. Before executing conversion, specify the oscillation range and detector distance used for the dataset in the command line [13].

2. Visualize the images using Adxv to cycle through the converted frames. Select an appropriate image to use for identification of the beam center (*see* **Note 15**) Repeat this process on several different images to obtain a more precise value.

3. Generate or download an appropriate XDS input template (http://xds.mpimf-heidelberg.mpg.de/html_doc/xds_prepare.html).
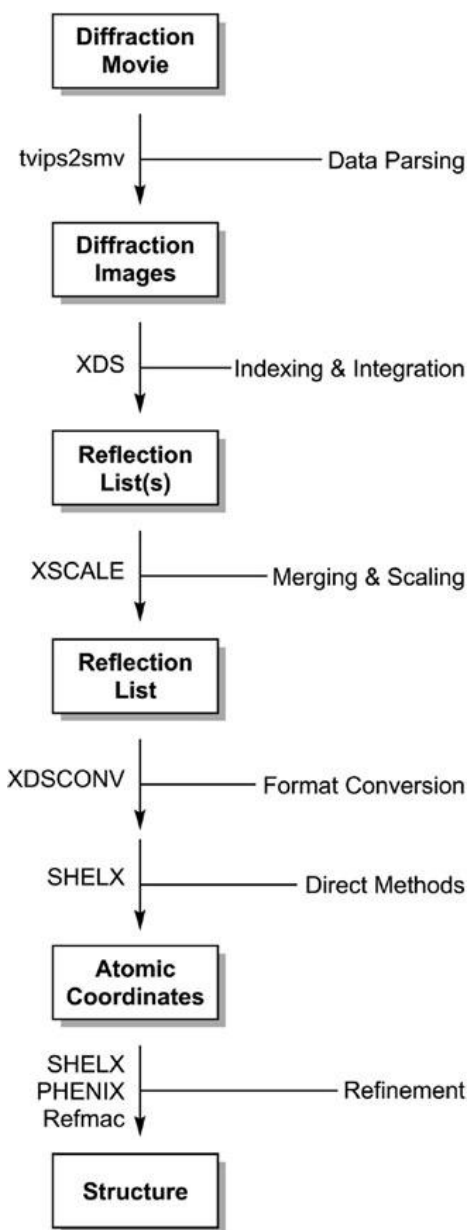
Fig. 3 Sample workflow for structure determination *via* direct methods. Subheading 3.3 covers diffraction; Subheading 3.4 covers indexing and integration; Subheading 3.5 covers merging, scaling, and format conversion; Subheading 3.6 covers direct methods and refinement

4. To specify the location of the beam center in a dataset, use the values calculated in **step 2** as the inputs for origin parameters in the XDS.INP file.

5. Enter the correct relativistic wavelength of the incident electron beam as the X-RAY_WAVELENGTH. This parameter is dependent on the specific accelerating voltage employed by the instrument (*see* **Note 16**).

6. Enter the correct ROTATION_AXIS values according to the direction of rotation and predetermined detector geometry, which differs by instrument.

7. Based on a visual inspection of the stack of diffraction images in Adxv, pinpoint the specific range of frames which incorporates the highest quality data to be used for indexing. Set SPOT_- RANGE as this set of frames. Avoid frames with visible defects such as polycrystalline reflections or overly elongated, ellipsoidal spots. DATA_RANGE specifies the range of images used for integration and can include all the frames specified in SPOT_RANGE and more.

8. Run XDS. If no errors occur, proceed to **step 9**. If errors appear, *see* **Note 17.**

9. The stringency of IDXREF may result in the frequent appearance of errors, prematurely halting further processing. If confidence in indexing is high, these halts can be circumvented by modifying the JOB settings in the XDS.INP input file as suggested by the error output and rerunning XDS (*see* **Note 18**).

10. Optimize the indexing solution by adjusting parameters such as the set of frames used for indexing and integration, the minimum number of pixels in a peak, the thresholds for background and peak pixel selection, and the mosaicity model (*see* **Note 19**).

11. Run XSCALE on the optimized indexing solution.

12. Repeat **steps 1–10** for each movie collected.

3.5 Dataset Merging

1. To merge datasets, create a new XSCALE.INP input file.

2. Specify the respective file paths of each desired XDS_ASCII. HKL file using INPUT_FILE (*see* **Note 20**).

3. Run XSCALE. Analyze the statistics of the merged solution in XSCALE.LP (*see* **Note 21**) (Fig. 4a).

4. Once a satisfactory merge is successfully implemented, open XDSCONV.INP and set the output type and file extension to SHELX and ".hkl," respectively.

5. Run XDSCONV to convert the scaled reflection file generated by XSCALE (with an ".ahkl" extension) to ".hkl" format. This renders it readable by SHELX.

6. Alternatively, open XDSCONV.INP and set the output type and file extension to CCP4_I+F and ".ascii," respectively. Run XDSCONV. XDSCONV may prompt the user for additional CCP4 commands to be executed, generating a binary list of reflections with the extension ".mtz".

7. Visualize the ".mtz" file (Fig. 4b) with viewHKL and search for systematic absences to aid in space group determination.
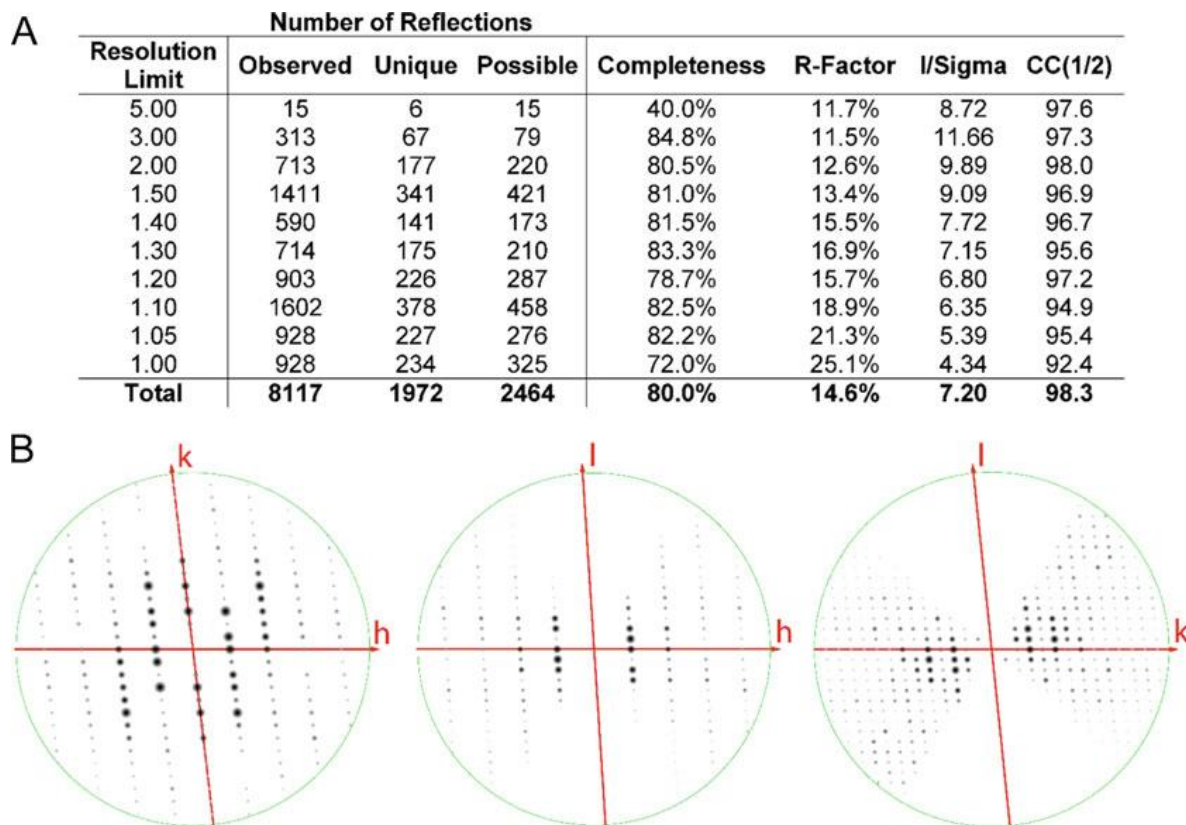
A

Resolution Limit	Number of Reflections			Completeness	R-Factor	I/Sigma	CC(1/2)
	Observed	Unique	Possible				
5.00	15	6	15	40.0%	11.7%	8.72	97.6
3.00	313	67	79	84.8%	11.5%	11.66	97.3
2.00	713	177	220	80.5%	12.6%	9.89	98.0
1.50	1411	341	421	81.0%	13.4%	9.09	96.9
1.40	590	141	173	81.5%	15.5%	7.72	96.7
1.30	714	175	210	83.3%	16.9%	7.15	95.6
1.20	903	226	287	78.7%	15.7%	6.80	97.2
1.10	1602	378	458	82.5%	18.9%	6.35	94.9
1.05	928	227	276	82.2%	21.3%	5.39	95.4
1.00	928	234	325	72.0%	25.1%	4.34	92.4
Total	8117	1972	2464	80.0%	14.6%	7.20	98.3

B

Fig. 4 Data reduction statistics for the merging and scaling of partial datasets from six peptide crystals (**a**). This example demonstrates reduction of data in the lowest symmetry space group, P1. The lack of symmetry is confirmed by a lack of systematic absences along *hkl* zones of the merged and scaled data (**b**; *l* = 0 left, *k* = 0 middle, *h* = 0 right) in ViewHKL

3.6 Structure Determination

1. Generate a SHELX instruction file (extension ".ins") by using SHELXPRO [26] (*see* **Note 22**).

2. Execute SHELXD/T with the newly made instruction file and the list of reflections generated in **step 5** in the previous section (".hkl"). During the SHELX trials, keep track of the best CFOM values; these form a distribution whose high end may be indicative of correct solutions (Fig. 5) (*see* **Note 23**).

3. Open the direct methods solution in Coot (".pdb" or ".res" files tolerated) or PyMOL (accepts ".pdb" files) to visualize the atoms. Generally, a solution is considered valid when each atom in the polypeptide backbone is placed in accordance with well-established restraints on bond geometries (Fig. 6a).

4. While structure determination programs do not routinely assign the absolute configuration of individual stereocenters from electron diffraction data, special routines can be implemented to exploit potential differences in Friedel mates [33]. In the event that absolute structure is known but SHELXD/T outputs its inverse, the PDBSET program [29] can rectify the handedness of the coordinate file by inverting the input coordinates.
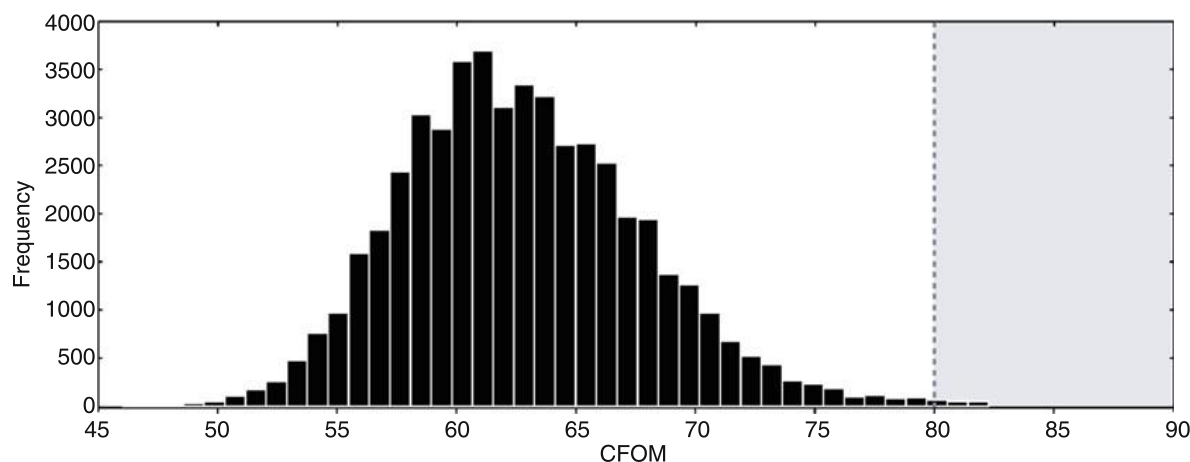
Fig. 5 Histogram of the combined figure of merit (CFOM) scores for 50,000 trials by SHELXD, indicating the approximate frequency of correct solutions. The shaded region, where CFOM scores exceed 80 [6], represents an area in which solutions have a high probability of being correct

5. SHELXL can use the original list of reflections and the atomic coordinates outputted by SHELXD/T to generate a density map for model building. Make a copy of the ".res" output from SHELXD/T and rename it as an ".ins" file. Now rename the ".hkl" file used for direct methods calculations so that it matches the new ".ins" file. Run SHELXL, calling the new ".ins" and ".hkl" files as inputs. This will produce a calculated density map as an ".fcf" file (also readable in Coot).

6. Build a polypeptide model in Coot or PyMOL by sequentially assigning specific residues according to the data (Fig. 6b).

7. Refine the structure using the newly built model in tandem with the original list of reflections supplied by XDSCONV in **step 5** of Subheading 3.5. Several standard programs can execute refinement; Phenix and REFMAC natively support electron scattering factors (*see* **Note 24**).

4 Notes

1. Recommended instruments employ field-emission guns (FEGs) as electron sources. These contain elemental tungsten (W) tips roughly 15 nm in diameter coated with a thin layer of zirconium oxide (ZrO). The apex of the emitter approaches 1800 K during excitation, augmenting ZrO conductivity and facilitating thermionic emission by diminishing the work function of the cathode. Schottky-type FEGs generate a highly coherent beam, with an energy spread ΔE of 0.3–0.7 eV. Alternative sources such as W hairpin filaments or lanthanum hexaboride crystals exhibit ΔE values of 1.5–3 eV and 1–2 eV, respectively. Systems operating at a higher accelerating voltage
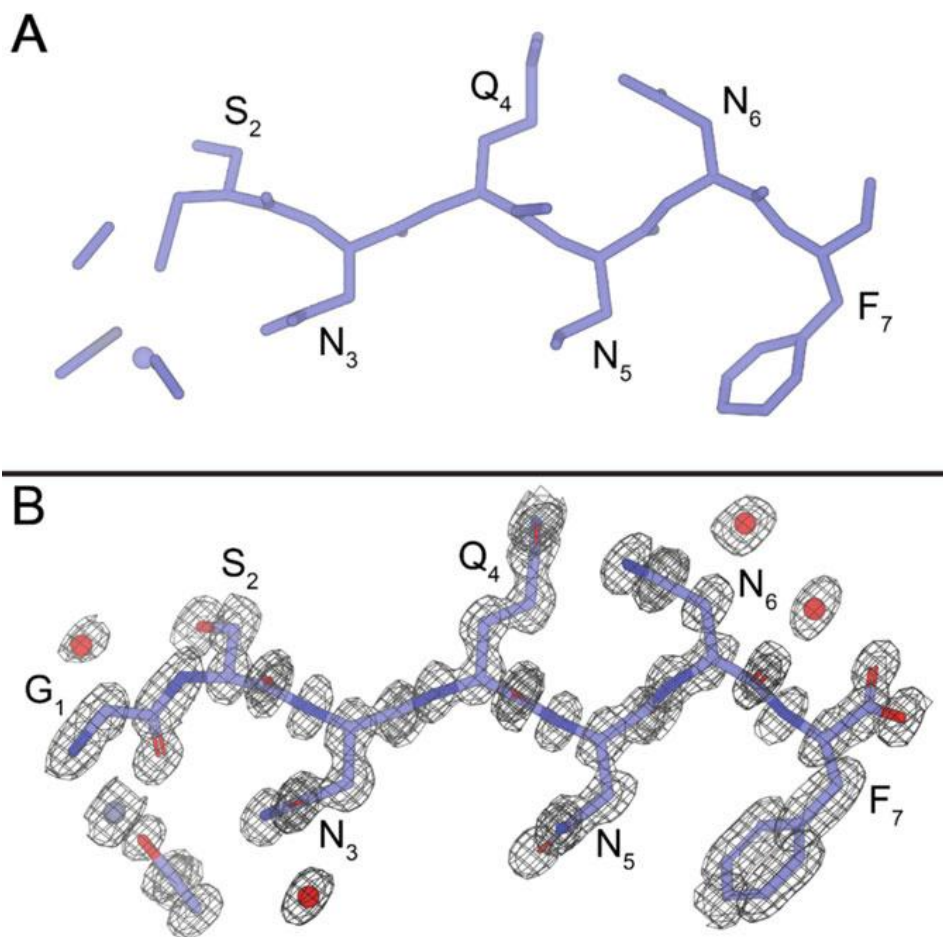
Fig. 6 Ab initio atomic coordinates of L-GSNQNNF outputted by SHELXD (**a**) and the corresponding atomic coordinates refined by Phenix (**b**). The $2F_o–F_c$ map, represented by the black mesh, is contoured at 1.2 σ. Modelled water molecules are present as red spheres, with hydrogens omitted for clarity. The final structure has an R_{work} of 0.172 and an R_{free} of 0.205

are preferred since these can also accommodate lower accelerating voltages (i.e., a 300 keV instrument can be driven at 200 keV if necessary). Although cold FEGs (in instruments such as the JEOL JEM-2100) can achieve even better spatial coherence, Schottky-type FEGs may offer greater durability, lower noise, and steadier beam current [34].

2. Other detectors include the CMOS-based CetaD 16 M (Thermo Fisher Scientific, [35]), a previous generation TVIPS TemCam-F416 (Tietz Video and Image Processing, [13]), and two direct electron detectors, Falcon in integrating mode [35] and K2 in counting mode (Gatan Inc., [36]). Hybrid pixel detectors such as the Dectris EIGER detector [37] and the Medipix2 [38] allow for fast and high dynamic range data collection. In principle, collection of MicroED data using a slow-scan CCD is possible, but inherent deficits in readout speed may severely limit data quality.

3. Because continuous rotation of the sample stage during MicroED is analogous to rotation of a mounted crystal on an X-ray diffractometer, software originally developed for X-ray crystallography can also process MicroED data. However, numerous parameters and settings (e.g., the wavelength of the incident radiation and the values of the relevant atomic scattering factors) must be adjusted accordingly to account for the discrepancies between X-rays and electrons.

4. To avoid redundancy, we minimize our description of procedures that may be more extensively covered by other chapters. Please refer to other chapters in this volume for a more thorough explanation of these topics and/or procedures.

5. Due to liquid nitrogen's relatively low heat capacity, samples plunge-frozen in liquid nitrogen often suffer from co-crystallization of adventitious ice. This is because interaction with the room-temperature sample causes an insulating layer of nitrogen to evaporate immediately upon contact as described by the Leidenfrost effect, prolonging the flash-freezing process and allowing water sufficient time to crystallize. Conversely, liquid ethane exhibits much higher heat capacity and therefore functions as a ruthlessly efficient cryogen that captures samples in vitreous ice. However, this property also renders it far more hazardous. Liquid ethane causes severe cryogenic burns immediately upon contact with exposed skin. When condensing ethane, exercise extreme caution and wear appropriate personal protective equipment, such as cryogenic gloves and eye protection.

6. Certain types of EM grids exhibit incompatibility with particular solvents. For example, formvar, a common plastic support film, is soluble in chloroform, dichloroethane, and 1,4-dioxane. Also, copper and some other metal meshes are highly susceptible to degradation by acids and bases.

7. Some cryo-protectants can increase the difficulty of an experiment by obstructing blotting efficiency. In general, an evaluation of solvent choice and sample compatibility with grids and freezing conditions prior to sample deposition is critical. For example, certain materials routinely used in X-ray diffraction can be incompatible with conventional sample preparation for MicroED. Common, non-volatile cryoprotectants (such as paratone oil, sucrose, trimethylamine N-oxide (TMAO), lipidic cubic phases, and perfluoropolyether oils) can cause particular challenges for both freezing and sample interrogation by an electron beam.

8. The size of the beam will determine the flux on the sample in electrons per Ångstrom squared. An image of the electron beam propagating through vacuum can help estimate the dose at low electron counts.

9. To calibrate the diffraction stigmator, adjust the C2 lens intensity. A fully condensed beam sits at a crossover point: adjusting the C2 intensity in either direction should result in an expansion. The beam should expand and collapse concentrically as a nearly circular ellipse. Shape distortions should be corrected by adjusting the console multifunction knobs while the stigmator adjustment icon is active.

10. While the XF416 detector is capable of full-chip readout at nearly 50 frames/s, not all applications warrant this readout speed. In particular, certain applications such as shutter-free data collection may benefit from slower readouts that limit the accumulation of readout noise. Likewise, spatial subsampling or binning of the collected frames can enhance signal over noise. The collection strategies described here rely on 2×2 binning of full-frame diffraction images, but larger binning can be employed if desired, with a caveat. Binning reduces sampling of the reciprocal lattice and therefore constrains measurements, as lattice spacings shrink and reflections risk being overlapped. This is also influenced by the selected camera length as described in the following note.

11. The ideal detector distance places the finest resolution reflections at or near the edge of the detector, maximizing the collection of reflections at both coarse- and fine-resolution shells. Crystals with larger unit cell dimensions will exhibit a more compact reciprocal lattice and require longer detector distances to prevent overlapping spots from affecting integrated intensities, which is influenced by detector sampling of the reciprocal lattice.

12. Visual obstruction of the sample by grid bars, other crystals, or debris is commonplace at high tilts, effectively limiting the upper and lower bounds of rotation. Keep in mind that as the x- and y-axes approach the stage's outer boundaries, high-angle tilts become more likely to cause physical collisions between the microscope and the sample holder.

13. Coordination of stage rotation with diffraction data collection requires intervention. The software module controlling stage rotation can be accessed through the Temspy dialog box, under dialogs, CompuStage. The parameters for saving recorded movies can be set by accessing the Recorder Settings dialog box from the toolbar menu. Video capture occurs by pressing the camcorder icon on the EMMenu4 user interface after having set a desired integration time per frame. A second icon (red record button on the EMMenu4 user interface) allows for storage of the captured video frames when pressed as video is being captured.

14. To achieve optimal data quality, parameters such as camera length, continuous rotation rate, exposure time, and crystal orientation must be judiciously selected. A rotation rate of 0.1°–0.5°/s is recommended. Faster oscillations may result in overlapping spots, while slower oscillations may result in an insufficient number of spots due to sample degradation over time. Additionally, exposure times between 0.1 and 10 s are recommended. Longer exposures can increase the signal-to-noise ratio, but may place reflections from large unit cells in danger of overlapping, even at slow oscillations. Data from crystals that demonstrate orientation bias when deposited on a grid is limited in its sampling of reciprocal space (i.e., via collection of diffraction patterns at high tilt). Sufficient sampling is critical for obtaining high-completeness data.

15. Several procedures exist for identifying the location of the beam center in a diffraction image. We describe a procedure based on the relationship between the approximate locations of Friedel mates. Here, one would draw lines connecting pairs of Friedel mates to estimate the spatial coordinates of the beam center. The position of the beam center may change or drift between or within datasets. If this occurs, recalculate its value accordingly.

16. XDS requires the user to supply the wavelength of the incident radiation. While this is denoted X-ray for historical reasons, its name has no bearing on the calculations performed by the program. Calculation of this key parameter is straightforward for X-rays (characteristic values include 0.7107 Å for Mo Kα and 1.5418 Å for Cu Kα). In contrast, typical TEM accelerating voltages (i.e., >100 keV) suitable for MicroED produce a high-energy beam in which each constituent electron is forcibly propagated through a potential drop, ultimately generating a beam of quanta traveling at a velocity greater than half the speed of light. Therefore, an accurate calculation of the electron wavelength must incorporate relativistic contraction, as follows:

$$\lambda = \frac{h}{\sqrt{2m_0\mathrm{eV}\left(1 + \frac{\mathrm{eV}}{2m_0c^2}\right)}}$$

In the above equation, h is Planck's constant, m_0 is the rest mass of the electron, eV is the kinetic energy imparted by the accelerating voltage, and c is the speed of light in a vacuum. *See* Table 1 for characteristic values for the relativistic wavelength of the incident electron beam, which include 0.0251 Å at 200 keV and 0.0197 Å at 300 keV [34]. Discrepancies between the relativistic and non-relativistic calculations widen significantly as the accelerating voltage rises. Furthermore, recall that

Table 1
Relativistic and non-relativistic electron wavelengths at energies usable in MicroED experiments [41]

Accelerating voltage (keV)	Non-relativistic wavelength (Å)	Relativistic wavelength (Å)	Percent error (%)
100	0.0386	0.0370	4.15
120	0.0352	0.0335	4.83
200	0.0273	0.0251	8.06
300	0.0223	0.0197	11.66
400	0.0193	0.0164	15.03

the radius $1/\lambda$ of the corresponding Ewald sphere scales inversely with the wavelength of the incident quanta. As a result, given the markedly shorter wavelengths inherent to electron diffraction, the curvature of the Ewald sphere is flattened, and its gently sloping arc is reliably approximated as a plane at >100 keV. (This stands in stark contrast to X-ray diffraction, in which the geometry of the Ewald sphere stays true to its name.) Each observed reflection represents a cross-section between the surface of the Ewald sphere and a reciprocal lattice vector. Therefore, a wide, flattened Ewald sphere can in principle accommodate many reciprocal lattice points per angle. In practice, this advantage is attenuated by the restricted tilt range available to TEM instruments.

17. If IDXREF produces an error beginning with "INSUFFICIENT PERCENTAGE (<50%) OF INDEXED REFLECTIONS," proceed to **step 9**. If XDS fails to find an adequate indexing solution ("IER = 0"), inspect the values for the parameters set in **steps 3–5**. Specifically, consider supplying a different range of frames for SPOT_RANGE. If XDS cannot determine an adequate indexing solution after multiple iterations of adjustments, it may indicate poor data quality.

18. The IDXREF error described in **Note 17** may be caused by many factors, including a limited tilt range. Unlike a multi-axis goniometer, TEM instruments exhibit a restricted range of motion. Thus, MicroED datasets may not always include a large number of reflections within a given wedge of reciprocal space, leading to indexing ambiguities. Other potentially causative factors include non-eucentric sample rotation and lens aberrations [18].

19. Statistical analysis of each processing task implemented by XDS (such as IDXREF) is stored in its respective log file (with an ". LP" extension, such as IDXREF.LP). These log files contain a preponderance of potentially useful information which could enhance or facilitate an indexing solution. As an illustrative

example, CORRECT.LP supplies detailed statistics describing several alternative solutions generated by indexing smaller subsets of frames within the previously specified SPOT_RANGE. This provides insight into which specific set of frames is truly ideal for SPOT_RANGE.

20. Due to hardware restrictions imposed by the instrument, individual MicroED datasets rarely yield sufficiently high values of overall completeness to generate tractable direct methods solutions on their own. Merging several datasets can compensate for this. For n independent datasets, there exist 2^n-1 unique ways to exhaustively merge them together. Note that XSCALE can also truncate each individual dataset at a given resolution range using INCLUDE_RESOLUTION_RANGE. Only select individual datasets that generate highly convergent indexing solutions (i.e., datasets which exhibit strong agreement in parameters such as unit cell dimensions and Laue symmetry). Forcibly merging inherently discordant datasets will undeniably prove fruitless.

21. Obtaining an optimal dataset may require systematic screening of parameters (i.e., adjusting resolution range, re-indexing individual movies, and merging disparate combinations of movies) to improve statistics. Attempt to minimize R-factors and maximize completeness and I/SIGMA. For an example of the summary statistics produced by XSCALE, *see* Fig. 4.

22. Many methods exist for generating instruction files for SHELXD. For example, a custom program (referred to here as shelxdpro) can facilitate direct methods solutions of protein/peptide structures. To achieve this, shelxdpro prompts users for information needed to generate instruction files for running SHELXD or SHELXT. First, shelxdpro prompts the user to enter the protein sequence, the space group number, and the unit cell parameters. Shelxdpro uses this information to calculate Matthews coefficients and suggest feasible choices for the number of molecules in the asymmetric unit. The user selects a value, and then shelxdpro calculates the number of carbons, nitrogens, oxygens, and other atoms required to write the SFAC, UNIT, FIND, and PLOP statements. Lastly, shelxdpro asks for the name of the SHELX formatted diffraction data file (.hkl) for this project and an indication of whether the file contains amplitudes or intensities. Shelxdpro writes this information, including space group operators in a format that SHELXD/T accepts. The user can use this instruction file to run SHELXD/T immediately. The benefit of such a program is time savings in omitting a search inputs such as space group operators and number of atoms of each element in the unit cell. Such a program also relieves the user of remembering the cryptic lattice code specific to the space group and eliminates the possibility for formatting errors.

23. SHELXD requires the user to supply an exact space group for direct methods and is therefore unlikely to yield a reasonable solution if the user's prediction is incorrect. Conversely, SHELXT extracts the Laue symmetry of the indexing solution and determines the space group through multiple considerations [39]. Depending on the number of atoms, solutions with a combined figure of merit (CFOM) greater than 80 will have a high probability of being correct (Fig. 5).

24. Programs such as SHELXLE require manual input of electron scattering factors as SFAC commands [40]. Due to artefacts unique to electron diffraction, the R-factors of refined MicroED structures generally exceed those of their X-ray counterparts. An acceptable solution could exhibit R_{work} and R_{free} values near or less than 0.25, with a split below 0.05 (Fig. 6b).

Acknowledgments

References

1. Shi D, Nannenga BL, de la Cruz MJ et al (2016) The collection of MicroED data for macromolecular crystallography. Nat Protoc 11:895–904

2. Shi D, Nannenga BL, Iadanza MG et al (2013) Three-dimensional electron crystallography of protein microcrystals. elife 2:e01345

3. Rodriguez JA, Eisenberg DS, Gonen T (2017) Taking the measure of MicroED. Curr Opin Struct Biol 46:79–86

4. Jones CG, Martynowycz MW, Hattne J et al (2018) The cryoEM method MicroED as a powerful tool for small molecule structure determination. ACS Cent Sci 4:1587–1592

5. Rodriguez JA, Ivanova MI, Sawaya MR et al (2015) Structure of the toxic core of α-synuclein from invisible crystals. Nature 525:486–490

6. Sawaya MR, Rodriguez J, Cascio D et al (2016) Ab initio structure determination from prion nanocrystals at atomic resolution by MicroED. PNAS 113(40):11232–11236

7. Zee C, Glynn C, Gallagher-Jones M et al (2019) Homochiral and racemic MicroED structures of a peptide repeat from the ice-nucleation protein InaZ. IUCrJ 6:1502238

8. Gallagher-Jones M, Glynn C, Boyer DR et al (2018) Sub-ångström cryo-EM structure of a prion protofibril reveals a polar clasp. Nat Struct Mol Biol 25:131–134

9. de la Cruz MJ, Hattne J, Shi D et al (2017) Atomic-resolution structures from fragmented protein crystals with the cryoEM method MicroED. Nat Methods 14:399–402

10. Guenther EL, Cao Q, Trinh H et al (2018) Atomic structures of TDP-43 LCD segments

and insights into reversible or pathogenic aggregation. Nat Struct Mol Biol 25:463–471

11. Hughes MP, Sawaya MR, Boyer DR et al (2018) Atomic structures of low-complexity protein segments reveal kinked β sheets that assemble networks. Science 359:698–701

12. Hattne J, Shi D, Glynn C et al (2018) Analysis of global and site-specific radiation damage in cryo-EM. Structure 26:759–766.e4

13. Hattne J, Reyes FE, Nannenga BL et al (2015) MicroED data collection and processing. Nat Struct Mol Biol 71:353–360

14. Palatinus L, Brázda P, Boullay P et al (2017) Hydrogen positions in single nanocrystals revealed by electron diffraction. Science 355:166–169

15. Zou X, Hovmöller S, Oleynikov P (2011) Electron crystallography: electron microscopy and electron diffraction. Oxford University Press, Oxford

16. Zuo JM, Spence JCH (2017) Advanced transmission electron microscopy: imaging and diffraction in nanoscience. Springer-Verlag, New York

17. Frank J (2006) Three-dimensional electron microscopy of macromolecular assemblies: visualization of biological molecules in their native state. Oxford University Press, Oxford

18. Heidler J, Pantelic R, Wennmacher JTC et al (2019) Design guidelines for an electron diffractometer for structural chemistry and structural biology. Acta Cryst D 75:458–466

19. Passmore LA, Russo CJ (2016) Specimen preparation for high-resolution cryo-EM. Methods Enzymol 579:51–86

20. Knapek E, Dubochet J (1980) Beam damage to organic material is considerably reduced in cryo-electron microscopy. J Mol Biol 141:147–161

21. Dubochet J, Adrian M, Chang J-J et al (1988) Cryo-electron microscopy of vitrified specimens. Q Rev Biophys 21:129–228

22. Jones C, Asay M, Kim LJ et al (2019) Characterization of reactive organometallic species via MicroED. ACS Cent Sci 5(9):1507–1513

23. Yonekura K, Ishikawa T, Maki-Yonekura S (2019) A new cryo-EM system for electron 3D crystallography by eEFD. J Struct Biol 206:243–253

24. Arvai A (2015) Adxv—A program to display X-ray diffraction images

25. Kabsch W (2010) XDS. Acta Crystallogr D Biol Crystallogr 66:125–132

26. Sheldrick GM (2008) A short history of SHELX. Acta Cryst 64:112–122

27. Adams PD, Afonine PV, Bunkóczi G et al (2010) *PHENIX*: a comprehensive Python-based system for macromolecular structure solution. Acta Cryst 66:213–221

28. Murshudov GN, Skubák P, Lebedev AA et al (2011) *REFMAC* 5 for the refinement of macromolecular crystal structures. Acta Cryst 67:355–367

29. Winn MD, Ballard CC, Cowtan KD et al (2011) Overview of the CCP4 suite and current developments. Acta Crystallogr D Biol Crystallogr 67:235–242

30. Emsley P, Lohkamp B, Scott WG et al (2010) Features and development of Coot. Acta Crystallogr D Biol Crystallogr 66:486–501

31. Delano W (2016) The PyMOL molecular graphics system. LLC, Schrödinger

32. Grassucci RA, Taylor DJ, Frank J (2007) Preparation of macromolecular complexes for cryo-electron microscopy. Nat Protoc 2:3239–3246

33. Brázda P, Palatinus L, Babor M (2019) Electron diffraction determines molecular absolute configuration in a pharmaceutical nanocrystal. Science 364:667–669

34. Reimer L, Kohl H (2008) Transmission Electron Microscopy: Physics of Image Formation. Springer-Verlag, New York

35. Hattne J, Martynowycz MW, Gonen T (2019) MicroED with the Falcon III direct electron detector. IUCrJ 6:921–926

36. Gallagher-Jones M, Ophus C, Bustillo KC et al (2019) Nanoscale mosaicity revealed in peptide microcrystals by scanning electron nanodiffraction. Commun Biol 2:26

37. Tinti G, Fröjdh E, van Genderen E et al (2018) Electron crystallography with the EIGER detector. IUCrJ 5:190–199

38. Nederlof I, van Genderen E, Li Y-W et al (2013) A Medipix quantum area detector allows rotation electron diffraction data collection from submicrometre three-dimensional protein crystals. Biol Crystallogr 69:1223–1230

39. Sheldrick GM (2015) SHELXT—integrated space-group and crystal-structure determination. Acta Crystallogr A Found Adv 71:3–8

40. Peng L-M (1999) Electron atomic scattering factors and scattering potentials of crystals. Micron 30:625–648

41. Williams DB (1996) Transmission electron microscopy—a textbook for materials science. Springer, New York. https://www.springer.com/us/book/9780387765006

INDEX